



Fine-scale ultralow-velocity zone structure from high-frequency seismic array data

Sebastian Rost,^{1,2} Edward J. Garnero,¹ and Quentin Williams³

Received 5 October 2005; revised 7 April 2006; accepted 2 June 2006; published 21 September 2006.

[1] Variability of core-mantle boundary (CMB) structure is imaged at the kilometer to tens of kilometers scale by intensive waveform modeling of the *ScP* phase. Recordings of earthquakes in the Tonga-Fiji subduction zone from the small-aperture (10 km), high-frequency ($\sim 2\text{--}4$ Hz) Alice Springs Array in central Australia are used to document anomalous *ScP* waveform variations due to the presence of an ultralow-velocity zone (ULVZ) at the CMB. These data expand coverage from previous results using the Warramunga Array, which is located slightly to the north, and indicate the existence of a geographically confined ULVZ at the CMB, roughly 100 km in lateral extent, south of New Caledonia and east of Australia. Synthetic modeling indicates seismic velocity reductions of $\sim 8\%$ and $\sim 24\%$ for *P* wave and *S* waves, respectively, and a well-constrained density increase of $\sim 10\%$ in a ~ 8.5 km thick layer above the CMB. This ULVZ patch is well explained by an elevated iron content of partially molten mantle material, likely present as divalent oxidized iron in the low spin state: The properties of such an iron-enriched assemblage are consistent with both an elevated density and bulk modulus of this region, as are dictated from our best fit seismic results. Furthermore, a positive velocity gradient within the ULVZ may be present, which need not be associated with a decrease in melt content within this region but could rather be associated with a shift in the textural distribution of melt within the ULVZ.

Citation: Rost, S., E. J. Garnero, and Q. Williams (2006), Fine-scale ultralow-velocity zone structure from high-frequency seismic array data, *J. Geophys. Res.*, *111*, B09310, doi:10.1029/2005JB004088.

1. Introduction

[2] Seismological studies over the last 50 years have detected a variety of structures at Earth's core mantle boundary (CMB) and in the overlying *D'* layer [Bullen, 1949] over scale lengths from 100 to 3000 km [e.g., Masters *et al.*, 2000; Garnero, 2000; Lay *et al.*, 2004; Lay and Garnero, 2004]. The detected structures include a sharp discontinuity at the top of the *D'* layer [e.g., Lay and Helmberger, 1983; Wysession, 1996; Wysession *et al.*, 1998] that appears well explained by a phase transition in lowermost mantle magnesium silicate perovskite [Murakami *et al.*, 2004; Oganov and Ono, 2004; Hernlund *et al.*, 2005; Lay *et al.*, 2005]. Additionally, anisotropy in the lowermost few hundred kilometers of the mantle [e.g., Kendall and Silver, 1998; Lay *et al.*, 1998; Kendall, 2000], strong scattering of seismic energy in the lowermost mantle [e.g., Bataille and Lund, 1996; Vidale and Hedlin, 1998], large-scale velocity reductions with sharp vertical boundaries between the anomalous structure and surrounding mantle

[e.g., Ni *et al.*, 2002, 2005], thin ultralow-velocity layering in the deepest 5–50 km of the mantle [e.g., see Garnero *et al.*, 1998; Rost and Revenaugh, 2003; Thorne and Garnero, 2004; Rost *et al.*, 2005], and evidence for localized rigid structures in the outermost fluid core [Buffett *et al.*, 2000; Rost and Revenaugh, 2001].

[3] Ultralow-velocity zones (ULVZ), with their uniquely strong seismic velocity reductions, are intriguing features of this apparently complex core-mantle transition region. Recent studies of ULVZ found reductions of *P* wave and *S* wave velocities of 5 to 15% and 10 to 40%, respectively [Garnero and Helmberger, 1998; Rost and Revenaugh, 2003; Thorne and Garnero, 2004]. Many studies have reported nondetections of ULVZ in large regions of the CMB, advocating that the ULVZ may not be a global layer, but rather intermittent [e.g., Garnero *et al.*, 1998; Castle and van der Hilst, 2000; Persh *et al.*, 2001; Thorne and Garnero, 2004]. However, some uncertainties and trade offs in ULVZ modeling are present. Thus the possibility exists for ULVZ presence in nondetection areas, with thicknesses below current detection levels (typically less than a few kilometers).

[4] High-resolution imaging of ULVZ structure, can be challenging, since only a few seismic phases can be used as ULVZ probes, and limitations in available source-receiver geometries are present. While the core wave *SP_{diff}KS* has been used to map ULVZ structure most extensively (amounting to roughly 40% of the CMB's surface area

¹Department of Geological Sciences, Arizona State University, Tempe, Arizona, USA.

²Now at School of Earth and Environment, University of Leeds, Leeds, UK.

³Department of Earth Sciences, University of California, Santa Cruz, California, USA.

[Garnero and Helmberger, 1998; Thorne and Garnero, 2004]), this probe does not uniquely constrain small-scale ULVZ structural details, primarily owing to an ambiguity between anomalous structure existing where P wave diffraction occurs in $SP_{diff}KS$ on the either the source or receiver-side of the wave path. An identical uncertainty is present for PKP precursors attributed to ULVZ structure and processes [e.g., Vidale and Hedlin, 1998]. Core-reflected phases (e.g., ScP (Figure 1a) and PcP), on the other hand, offer better spatial constraint and hence higher resolution in structural details, but the amplitudes of these phases are often small and in the noise level. However, seismic arrays allow for the possibility of raising amplitudes of coherent arrivals out of the ambient noise by stacking techniques [e.g., Vidale and Benz, 1992; Revenaugh and Meyer, 1997; Rost and Thomas, 2002]. Thus, with the increased availability of traditional seismic array data [e.g., Rost and Garnero, 2005], increased opportunities exist for deep earth investigations [e.g., Koper and Pyle, 2004].

[5] Recently, a high-resolution study of ULVZ structure using array recordings and analysis was able to resolve a laterally isolated ULVZ (roughly 50 km wide) with a 10% increase in the density of ULVZ material [Rost et al., 2005] (hereinafter referred to as R05). Here, in a similar approach, we use data from the small-aperture (10 km) Alice Springs Array (ASAR), in central Australia, which is part of the International Monitoring System (IMS [e.g., see Given et al., 2000]). The new data utilize earthquakes from the Tonga-Fiji and Vanuatu subduction zones, enabling us to interrogate an overlapping CMB region with R05 but using an independent data set of high-frequency ScP recordings with a slightly different source-receiver configuration (Figure 1b). ScP is well suited to study ULVZ layering [Garnero and Vidale, 1999] due to the generation of precursors and postcursors (phases with traveltimes less than and greater than ScP , respectively) due to conversions and reflections at the top of a ULVZ [e.g., Vidale and Benz, 1992; Reasoner and Revenaugh, 2000; Castle and van der Hilst, 2000; Persh et al., 2001; Rost and Revenaugh, 2001, 2003]. In what follows, we present ScP waveform anomalies from ASAR, waveform modeling, and constraints and uncertainties on the internal structure of the ULVZ. Finally we discuss insights into the modeled ULVZ chemistry development, evolution, and dynamics.

2. Short-Period ScP Array Data

[6] ASAR is a 19 element short-period seismic array with a maximum aperture of ~ 10 km (Figure 1b), about 300 km south of the Warramunga Array (WRA) used by R05. The array is part of the IMS to verify compliance with the Comprehensive Test Ban Treaty (CTBT) on underground nuclear explosions. These stations record short-period vertical component ground motion. The station configuration is optimized for analyses up to several hertz, although we note that signal coherency at teleseismic distances between stations degrades rapidly above 6 Hz. Instrumentation is identical for all array stations, so we have not removed the instrument response from the recorded data.

[7] Stations are distributed irregularly to obtain a δ function like array response function and to minimize side lobes in the receiver characteristics. Because of ASAR's

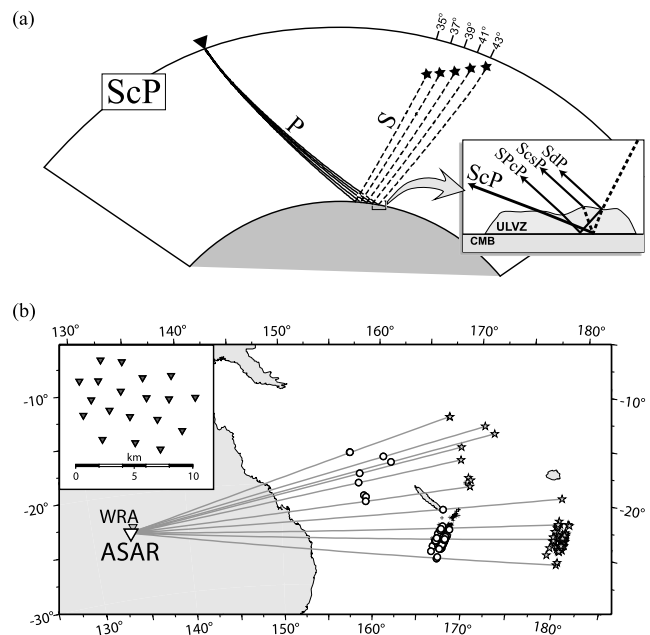


Figure 1. (a) ScP ray paths for epicentral distance of 35 to 43°. ScP starts out as a S wave (dashed) from the earthquake (stars), converting to a P wave (solid) upon CMB reflection and up to the station (triangle). Inset schematic shows possible additional arrivals due to reflections and conversions of S energy at the top of the ULVZ. (b) Source-receiver configuration for this study. Events (stars) are located in the Tonga Fiji subduction zone and are recorded at the small-aperture Alice Springs Array (ASAR), Australia (white triangle). Inset shows the configuration of ASAR instruments. The ScP CMB reflection locations for the PREM model [Dziewonski and Anderson, 1981] are shown by circles. Lines mark great circle paths between earthquakes and ASAR. The location of the Warramunga Array (WRA) is also shown (small gray triangle) for reference along with the CMB ScP sampling from the Rost et al. [2005] study region (crosses).

small aperture and smaller interstation spacing than WRA, it is more effective at retrieving shorter-period information than WRA due to higher signal coherency between stations at higher frequencies. We get the best slowness resolution and signal-to-noise ratio (SNR) for data band-pass filtered between 1 and 4 Hz. For comparison, R05 obtained best results for WRA data in the frequency band between 0.5 and 1.4 Hz. Studying ASAR data in this higher-frequency band holds promise to resolve smaller-scale structures at the CMB.

[8] We collected earthquakes from the time period January 1996 to December 2000, which can be freely downloaded through AutoDRM [Kradolfer, 1993] from the Center for Monitoring Research (CMR). We selected small ($m_b < 5.5$) and deep ($h > 200$ km) earthquakes. We obtained 116 events from the CMR with epicentral distances between 33.3° and 42.5° and source depths between 204 and 648 km. We find that the selected small events generally show simple impulsive source time functions, which is preferable for easier identification of precursors and postcursors to ScP due to interaction with ULVZ structure. Deep earthquakes

are preferable to minimize the effects of the attenuating upper mantle on the S leg of ScP which can reduce overall ScP amplitudes. Additionally, the arrival times of ScP and PcS are separated for deep earthquakes, which allows us to avoid waveform complications from simultaneous arrival of these two phases. The direct P wave was used to identify and retain events with simple source time functions, and ScP SNR was evaluated, keeping only high SNR data.

[9] The ASAR data are band-pass filtered between 1 and 4 Hz, then beam formed [Rost and Thomas, 2002] with respect to ScP slowness and back azimuth. The beam forming increases the amplitude of coherent ScP energy over incoherent noise. Coherent arrivals with differing slownesses (or incidence angles) will also be suppressed. Slowness and back azimuth are computed for any arrival near the predicted ScP time, which precludes possible false interpretation of other phases (such as from a different earthquake). From the original data set of 116 events, we remove recordings with complicated P source time functions and low ScP signal-to-noise ratio. This reduces the data set to 56 events. Table S1 in the auxiliary material gives the source locations for these events.¹

[10] We observe strong waveform variations in the precursor wavefield similar to those reported by R05. Figure 2 shows data examples for the three observed cases: events with no ScP precursor detection (Figure 2a), recordings with dominant ScP precursors detected (Figure 2b) and earthquakes with complicated ScP and precursor wavefield (Figure 2c). Figure 2d shows a profile of ScP beam traces sorted by back azimuth, which is essentially a south-to-north sorting of the data. The beam traces are aligned in time on the ScP onset and normalized to the ScP amplitude. ScP onsets are picked by hand since large delays of the ScP arrival with respect to reference model prediction prevent automated alignment, and slight pulse shape variances (particularly in the later part of ScP) prevent confident cross-correlation schemes for alignment. The profile shows that the ScP traces possessing clear precursors fall within a very small back azimuth ($99.5^\circ \leq \Theta \leq 100.5^\circ$) range, i.e., within a thin latitudinal band in the north-south sampling swath. The complicated (large amplitude) precursor data sample the CMB in a very small region just to the south of CMB sampling of data with clear precursor arrivals. This central region is surrounded by ScP sampling that lack evidence for clear precursors. All individual beam traces for these three groups are shown in Figures 2e–2g.

[11] The ScP precursors are indicative of the existence of ULVZ structure at ScP CMB reflection points; the data of Figure 2e sample an isolated zone (Figure 3) that is in good agreement with the earlier WRA study [R05]. The ASAR data allow us to investigate ULVZ structure further to the southeast than was possible using WRA data, and gives further constraints on the extension of this ULVZ of the R05 study (Figure 3). Four ScP reflections sample the CMB further to the west of the main detection area. ScP waveforms for these earthquakes are very similar to the double beamed waveform of the main detection area. Our data set does not allow us to prove whether this is one larger,

connected ULVZ or if the western events probe a second closely spaced ULVZ.

3. ScP Waveforms

[12] The back azimuth plot of Figure 2d represents a north-south (N-S) profile through the study area. We notice strong waveform variations along this $\sim 3^\circ$ N-S profile (~ 180 km) along the CMB. The change from earthquakes showing simple ScP waveforms to precursory events occurs within a few kilometers (definitely within the size of the Fresnel zone of ScP). The Fresnel zone for the 1 to 4 Hz data is about 1.5° by 1.5° at the ScP reflection point. The change at the southern boundary of the precursory region is less abrupt and some waveforms show evidence for strong focusing of the precursory energy, perhaps due to multipathing in the ULVZ structure. Double-beamed traces for the three regions (precursor, nonprecursor, and complex) are shown as bottom traces of Figures 2a–2c. For double beaming, we sum the beam formed traces for the three regions after aligning on the ScP arrival. This increases the SNR of the data further. The alignment on the ScP onset removes any time shifts due to different source depth of epicentral distance. It is obvious that no coherent energy arrives prior to the ScP arrival in case of the nonprecursor events (Figures 2a and 2f). The double beamed precursor data (Figures 2b and 2e) show precursory energy arriving ~ 1.9 s before ScP with about 10% of the ScP energy. These parameters are very similar to the ones found with WRA data [R05]. The four earthquakes characterized as complex (Figures 2c and 2g) show much higher precursor amplitudes of about 22% of ScP . Because of the fewer events going into the double beam, the SNR of this stack is not as high as in case of the precursor events. The main ScP waveforms within the three groups are highly coherent (see bottom traces in Figures 2e–2g). We also notice only very slight variations in the waveforms of the nonprecursors events, indicating very similar source time functions of the selected events and little variation of the CMB structure outside of the detected ULVZ. The differential traveltime and the precursor amplitude of all beam traces of the precursor events are in good agreement, with only slight variations.

[13] The detected precursor waveforms are in good agreement to the earlier study using the slightly longer period WRA data (Figure 4). The two independent data sets agree well both in amplitude and traveltime of the first precursor (SdP). A direct comparison of waveforms is difficult due to the different frequency content of the double beam traces. To provide a better comparison between the two data sets, Figure 4b compares the WRA data to the ASAR double beam low-pass filtered to match frequency content of the WRA double beam. The low pass was selected to provide a best fit between the main ScP waveform of the WRA and ASAR double beams. Filtering the ASAR double beam in this fashion leads to a striking similarity of the precursory wavefield, indicating that both data sets indeed sample the same CMB structure. The difference between the waveforms after the main ScP arrival is likely due to slight differences between the crustal/substation structure beneath WRA and ASAR.

[14] Because of the higher frequency of the ASAR double beam (than that of WRA), the temporal resolution of the

¹Auxiliary materials are available at <ftp://ftp.agu.org/apend/jb/2005jb004088>.

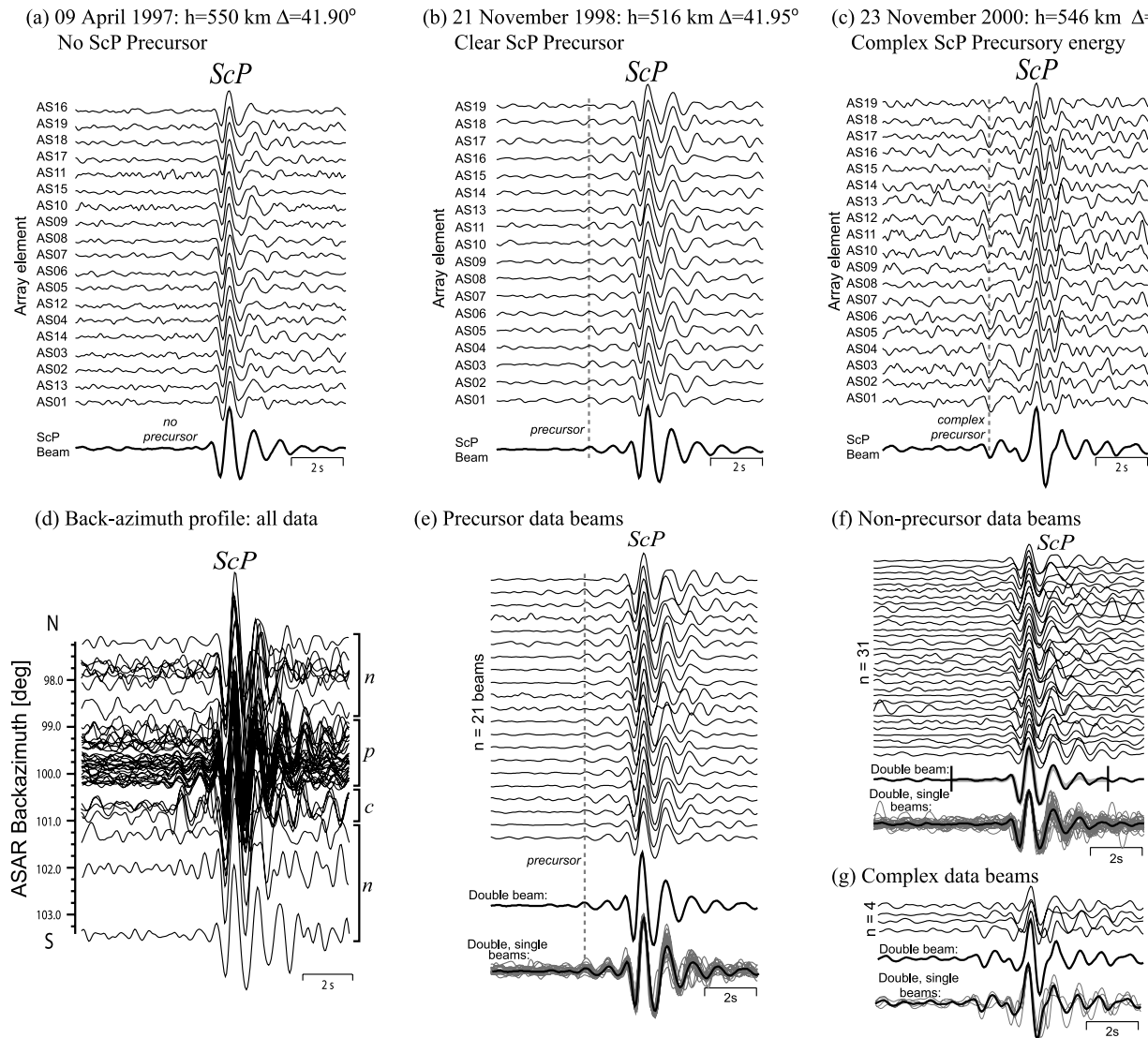


Figure 2. Band-pass-filtered data examples. (a) ASAR recordings for event on 9 April 1997 (top traces) which do not show precursory energy from ULVZ. Bottom trace shows double beam of all nonprecursor traces of the data set (see also Figure 2f). (b) ASAR recordings for event on 21 November 1998 (top traces) showing a distinct precursor. Bottom trace shows double beam of all precursor traces of the data set (see also Figure 2e). (c) ASAR recording (top traces) of event 23 November 2000 which shows large-amplitude precursors probably due to multipathing in the ULVZ. Bottom trace shows double beam of all traces showing these high-amplitude precursors (see also Figure 2g). (d) North-south back azimuth profile of ASAR *ScP* beam traces, aligned in time and amplitude on *ScP*. Back azimuth areas recording nonprecursors traces (*n*), precursors double beams (*p*) and complex waveform behavior with large-amplitude precursors (*c*) are marked. (e) Beam traces of data showing precursory energy (top traces). Waveforms between the individual beams are very similar (compare overlay of individual beams and double beam in lowermost trace). (f) Same as Figure 2e but for nonprecursor data beams. The *ScP* wavelet that was used in the synthetic forward modeling is shown underlying the double beam of the nonprecursor data. Two vertical lines additionally mark the end of the *ScP* wavelet. (g) Same as Figure 2e but for complex waveform beams.

precursor field is higher and we see evidence for the arrival of both precursors in the *ScP* wavefield (*SdP* and *SPcP*) [Garnero and Vidale, 1999; Rost and Revenaugh, 2003] (see Figure 1a inset). The *SPcP* arrival in the WRA double beam is masked by the waveform interference of *ScP* and *SdP*. The higher temporal resolution of the ASAR data

permits higher resolution of ULVZ parameters in the forward modeling.

4. Synthetic Forward Modeling

[15] We use the Gaussian Beam method (GBM) [Cerveny et al., 1982; Weber, 1988] to model the *ScP* waveform

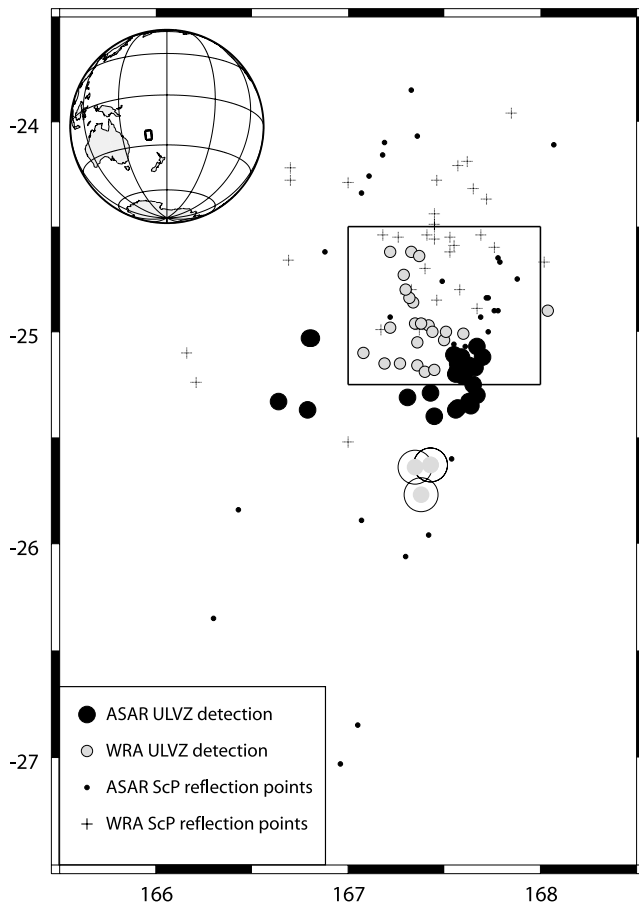


Figure 3. *ScP* reflection point locations for ASAR data set. Solid circles mark the reflection points of *ScP* showing precursory energy. Small solid circles denote events without waveform variations recorded at ASAR. The three shaded circles marked with additional solid circles south of the main ULVZ detections are events with complicated waveforms that are characterized as potential multipathing events. For reference, the results from *Rost et al.* [2005] using WRA data are also shown. Shaded circles mark *ScP* reflection point with precursor energy, while crosses show locations without waveform complication. The box marks the approximate location of the ULVZ detected by the earlier study. Inserted globe shows the location of the study area.

characteristics due to the interaction with ULVZ structure. We choose the GBM over full wavefield algorithms like the reflectivity method [Müller, 1985] due to the high-frequency of the data, which makes a full forward modeling using reflectivity not feasible due to extremely long calculation times. All major phases generated by the interaction between *ScP* and the ULVZ (*SdP*, *SPcP*, *ScP*, *ScsP*) are included in the modeling (for the arrival times of the additional phases relative to *ScP*, see *Rost and Revenaugh* [2003]). We find that higher-order multiples within in the ULVZ only contain minor energy and do not contribute significantly to the *ScP* waveforms. GBM calculates a spike train consisting of Gaussians with a width of 0.05 s which contains amplitudes, traveltimes and polarities of *ScP* and the additional arrivals. For exceedingly high frequencies, a

trade-off exists between the desired δ function and numerical stability for GBM, though we are able to stably compute *ScP* arrivals at the frequency of ASAR data. In contrast to earlier studies [e.g., *Rost and Revenaugh*, 2003], we use the *ScP* wavelet from the double beam of the nonprecursor events (Figure 2f) as an empirical source time function for our synthetic modeling. The tapered *ScP* wavelet is 5.8 s long and is shown underlying the *ScP* non-precursors double beam in Figure 2f. This source time function is convolved with Gaussian beam spike trains to obtain the synthetic seismogram for comparison with data. This source time function approach eliminates two problems that arise when using the double beamed *ScP* wavelet as source time function (e.g., as by *Rost and Revenaugh* [2001, 2003] and R05): (1) different *P* and *S* radiation patterns and different takeoff angles and (2) different paths of *P* and *ScP* and different attenuation along the path, each which can differentially affect the *P* or *ScP* waveshape, thus potentially contaminating results. We control the quality of the synthetic trace by comparing the synthetic *P* waveform with the appropriate *P* waveform in the data and find in general very good correlation between these two, showing the validity of this approach.

[16] The synthetic seismograms are calculated for a one-dimensional (1-D) Earth model, where the ULVZ is modeled as one layer at the bottom of the mantle with the overlying velocity model according to PREM. Although the ULVZ is likely a 3-D structure, we find that the waveforms of the *ScP* precursor events are very stable (Figure 2), indicating little change in ULVZ structure along the north-south ULVZ profile. This allows us to treat the problem in one dimension. Waveforms that sample the edge of the ULVZ and show evidence for multipathing have to be treated in a 3-D sense, which is currently not possible for the high frequencies used in this study.

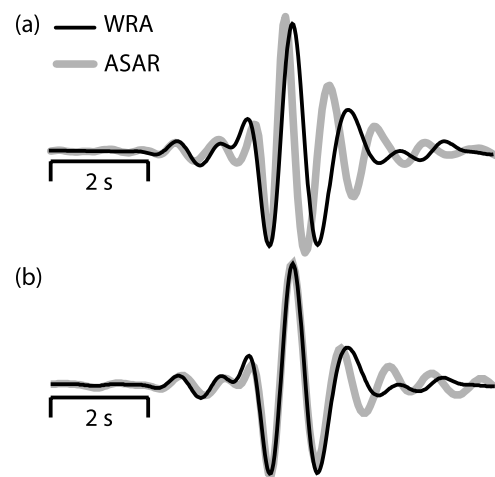


Figure 4. Comparison of WRA and ASAR double beams. (a) Data filtered with a 0.5 to 1.4 Hz band pass (WRA) and a 1 to 4 Hz band pass (ASAR). The ASAR double beam is shown as light gray line and the WRA data as black line. (b) Same as Figure 4a but with the ASAR double beam additionally filtered with a low pass to simulate the lower-frequency content of the WRA double beam.

[17] Figure 5 shows a collection of synthetic seismograms for varying ULVZ models. For these models the velocities and the density within the ULVZ are constant with depth. Three of the four parameters modeled (thickness D , P and S wave velocity reductions, δV_P and δV_S , respectively, and density change $\delta\rho$) are kept constant while one parameter is varied. A large parameter space is explored, where we vary ULVZ thicknesses between 4 and 18 km in 1 km increments, δV_P from 0 to 20% and δV_S from 0 to 40% in 1% and 2% increments. We include density variations from -10% to $+20\%$ in 1% increments. In general, we allow the parameters to vary independently, without presuming δV_P to δV_S velocity ratios or a specific density structure. All variations are relative to PREM [Dziewonski and Anderson, 1981]. Figure 5f shows models with a constant ratio between δV_P and δV_S ($\delta V_P:\delta V_S = 1:3$) while the absolute velocity reduction is varied; $\delta V_P/\delta V_S = 1/3$ is indicative for the existence of partial melt in the ULVZ [Williams and Garnero, 1996; Berryman, 2000] and is what has been found earlier by R05 for an ULVZ in this region. Nonetheless, we note that we do not restrict the search to models with fixed $\delta V_P/\delta V_S$ ratios.

[18] We control the fit between synthetics and data by calculating a residual trace by subtracting data from synthetics, taking the envelope of the residual trace and then integrate the remaining amplitude in a time window ± 5 s around the main ScP arrival. The misfit function weighs all parts of the waveform equally, while we find that a cross-correlation technique is mainly dominated by the larger-amplitude ScP . While this procedure does not give us any information about the location of the waveform misfit (i.e., which one of the precursors and postcursors is not well fit), it allows us a quantitative control on the overall wavelet fit. Misfit examples for varying ULVZ thicknesses and density are shown in Figure 6. The misfits for varying thickness show some scatter due to the periodicity of the signals. The thickness mainly changes the differential traveltimes between ScP and ULVZ generated phases. Depending on the traveltimes difference, the misfit changes strongly depending on the relative phase alignment between synthetics and data.

[19] From these experiments, we find that an 8.5 km thick ULVZ with an 8% P wave and 24% S wave velocity reduction and a 10% density increase gives the best fit between the ASAR data and the synthetics. We note though, that an 8 km thick ULVZ gives a similar good fit to the data. This is in very good agreement with the structure found by R05 supporting the finding of a dense, partially molten patch of material at the CMB. Nonetheless, we note that the density resolution from the ASAR data set is restricted (Figure 6c) and density increases between 6% and 10% relative to PREM give almost identical fits to the data. We find that the uncertainty on the ULVZ thickness is about ± 1 km, with about $\pm 3\%$ and $\pm 4\%$ uncertainty in P wave and S wave velocity reductions, respectively. The uncertainty on the density increase of the ULVZ is about $\pm 4\%$.

[20] The high-frequency content of the ASAR data set allows us to investigate the internal structure of the detected ULVZ in effort to better understand the constitution and development of these structures. Very few attempts have been made to resolve internal structure of ULVZ [e.g., Rondenay and Fischer, 2003], but none in this geographic

location, using core reflected phases. To resolve the internal velocity structure, the velocity jump at the upper boundary of the ULVZ is set to the best fitting values and a linear velocity gradient is assumed within the ULVZ (see insert of Figure 6d for a sketch of the P wave velocity profile). The synthetic tests using gradient ULVZ show that gradients ($\nabla(\delta V_P)$ and $\nabla(\delta V_S)$) of only one velocity (either P or S wave) strongly degrades the fit of the synthetics to the data. Figure 7 shows different fixed ratios for $\nabla(\delta V_P):\nabla(\delta V_S)$ of 1:1 and 1:3, which are characteristic for the composition of the ULVZ. The tests show that a further reduction of the velocities in the ULVZ results in a Hilbert transform of ScP , due to a caustic within the ULVZ layer, which leads to a severe degradation of the waveform fit (Figure 7). We can rule out these models, and accordingly a negative velocity gradient within the ULVZ itself is precluded. This result alone implies that a simple increase in melt content is unlikely to occur within the ULVZ, as would be expected if the ULVZ has a temperature increase with depth, and the ULVZ is solely generated by an intersection between the geotherm and the mantle solidus.

[21] Models with positive velocity gradients in the ULVZ show a variety of waveforms (Figure 7). We find an improvement of the fit relative to the best fit constant ULVZ for a model with a 4% P wave velocity and a 12% S wave increase within the 8.5 km of ULVZ (Figure 8). The best fitting gradient model shows a misfit between synthetics and data about 30% better than the best fitting constant velocity model (Figure 6). A close inspection of the waveforms shows that the improvement is mainly due to a better fit of the postcursor $ScsP$ (Figure 8a). However, we also note that the traveltimes and amplitudes of SdP and $SPcP$ are extremely well fit in the gradient model. It seems reasonable that the internal gradients follow a similar trend as the average ULVZ structure. We therefore did not test other combinations of internal gradients.

[22] We have systematically explored a vast synthetic model space that varied all parameters (ULVZ P and S velocity, density, thickness) over wide ranges, and were not able to improve upon the synthetic fit to the precursor/postcursor arrivals shown in Figure 8a without degrading the fit to the rest of the ScP waveform. We tested models including thin low-velocity lamellae a few kilometers above the CMB (e.g., as by Thomas *et al.* [1998]) and layered ULVZ models including two layers of velocity reductions [e.g., Rondenay and Fischer, 2003] but find that these models generate inferior waveform fits compared to the gradient models and the constant velocity one layer ULVZ. On the other hand, the linear gradient within the ULVZ might be a simplification of a more complicated velocity structure produced by the distribution of melt in the ULVZ: this possibility is discussed below.

5. Discussion

[23] Using higher-frequency data from a small-aperture high-quality array allows a higher resolution of the ULVZ layering at the bottom of the mantle. Tests with high-frequency reflectivity synthetics [Müller, 1985] constrain the thickness of the upper boundary of the ULVZ, i.e., the depth zone from which unperturbed mantle transitions to the partially molten ULVZ material, to be less than 500 m. A

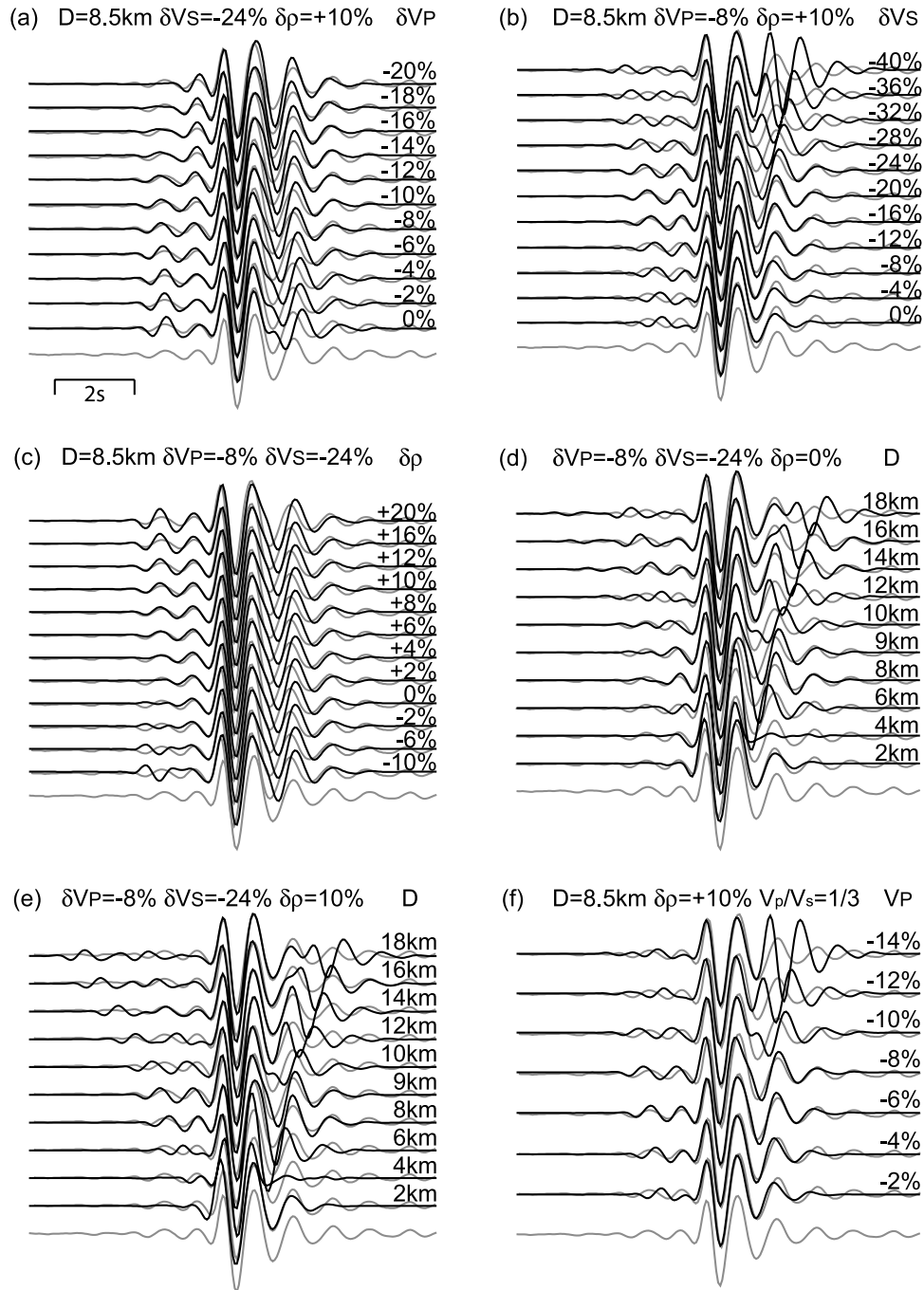


Figure 5. Gaussian beam synthetic seismograms for varying ULVZ models. Epicentral distance for the synthetics was chosen to be 41.5° , and a source depth of 550 km was assumed. Three parameters of the ULVZ are kept constant while one is varied. (a) ULVZ thickness ($D = 8.5$ km), S wave velocity reduction ($\delta V_S = -24\%$) and density change ($\delta\rho = +10\%$), while the P wave velocity change (δV_P) is varied. Lowermost gray trace shows recorded ScP double beam (also shown underlying the synthetic traces). (b) Same as Figure 5a but D , $\delta\rho$, and δV_P ($\delta V_P = -10\%$) are kept constant (and same as in Figure 5a) and δV_S is varied. (c) Same as Figure 5a but D , δV_P , and δV_S constant and density change $\delta\rho$ varied. (d) Same as Figure 5a but δV_P ($\delta V_P = -8\%$), δV_S ($\delta V_S = -24\%$), and $\delta\rho$ ($\delta\rho = 0\%$) are constant, while thickness D is varied. (e) Same as Figure 5a but δV_P ($\delta V_P = -8\%$), δV_S ($\delta V_S = -24\%$), and $\delta\rho$ ($\delta\rho = +10\%$) are constant, while thickness D is varied. (f) Ratio of δV_P and δV_S are kept constant ($\delta V_P:\delta V_S = 1:3$) but is varied from $\delta V_P = -2\%$ to -12% ($\delta V_S = -6\%$ to -36%), $D = 8.5$ km, and $\delta\rho = +10\%$.

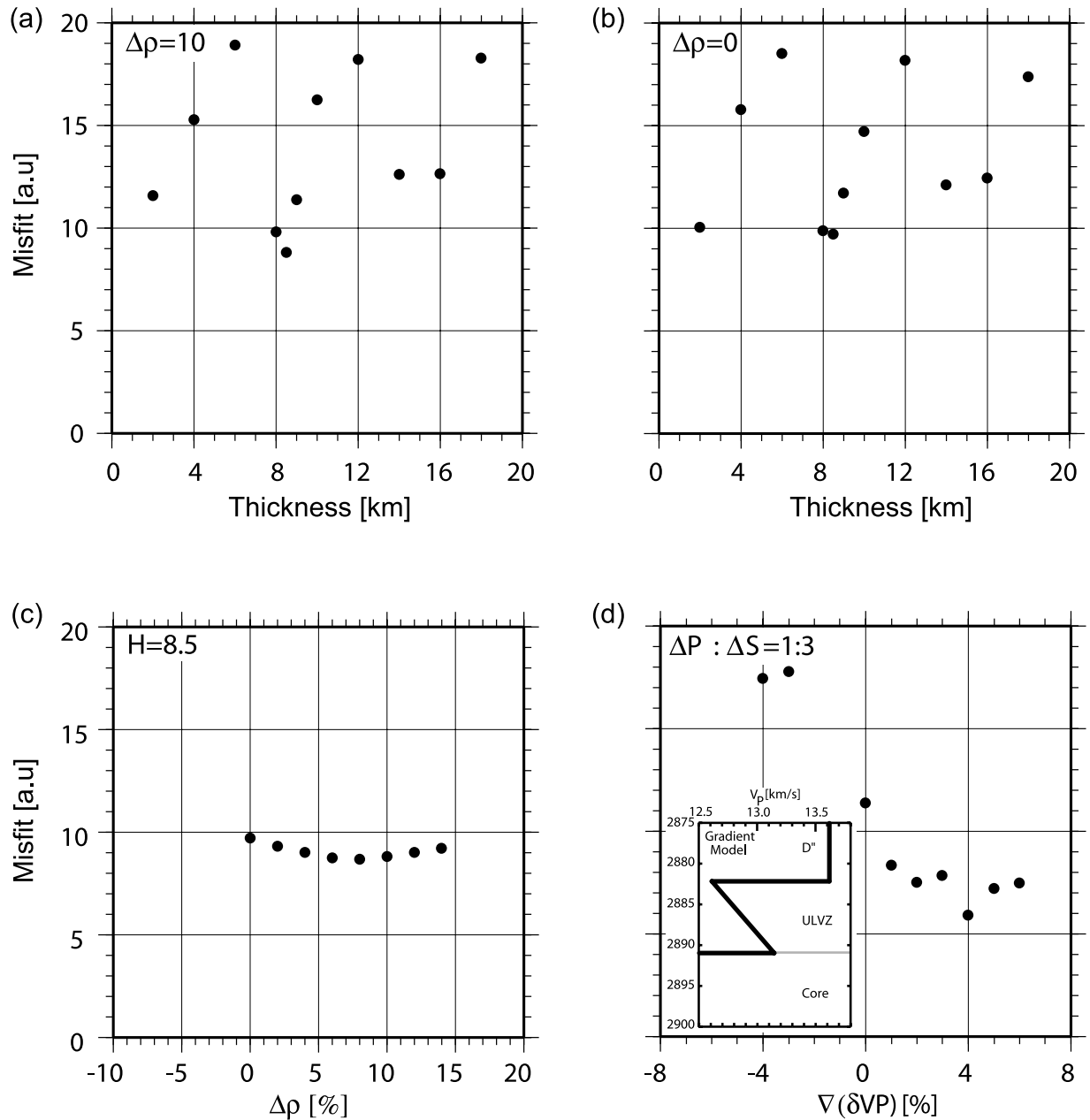


Figure 6. Misfit curves for synthetics. (a) Misfit between synthetic seismograms and precursor double beam trace. The model includes a ULVZ with 8% and 24% P wave and S wave velocity reductions, respectively, and a 10% density increase. Misfit is shown for varying ULVZ thicknesses. (b) As Figure 6a but for ULVZ without density increase ($\delta\rho = 0\%$). (c) Misfit for an 8.5 km thick ULVZ with 8% and 24% P wave and S wave velocity variations, respectively, and varying density. (d) Misfit for a $\nabla(\delta V_P) : \nabla(\delta V_S) = 1:3$ velocity gradient in the ULVZ, within a background of a 8.5 km thick ULVZ with 8% and 24% P wave and S wave velocity decreases, respectively, and a 10% density increase. Insert is a sketch of the P wave velocity profile in the gradient ULVZ model. The S wave model shows a similar trend.

larger transition results in rapid amplitude degradation of the precursory and postcuratory phases for the frequencies contained in the ASAR data. The source-receiver geometry of the ASAR data set locates the ULVZ slightly to the south of the previously detected patch by R05. However, the three-dimensional velocity structure of the mantle can also alter the ray paths of the seismic phases, which could

perturb our mapped location of this partially molten patch [e.g., see Zhao, 2001].

[24] The source-receiver geometry allows a sampling mainly along a north-south profile due to the location of the seismic sources in the Tonga-Fiji subduction zone. Therefore the detected ULVZ could be an extended ridge like feature instead of a circular, more constricted zone. ULVZ detections from WRA data [R05] extend the possible

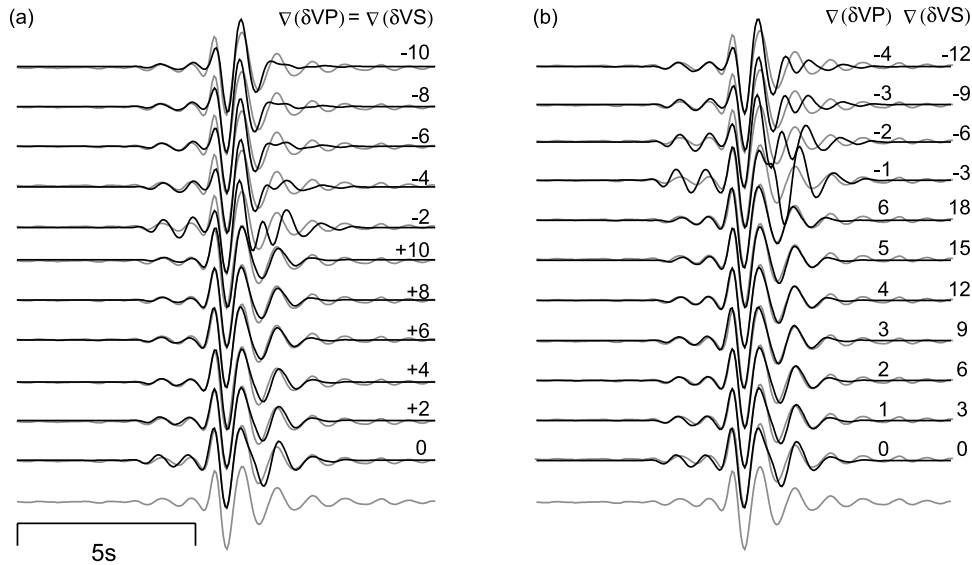


Figure 7. Synthetic test of internal velocity gradients in the ULVZ. As background model, an 8.5 km thick ULVZ with a -8% and -24% P and S wave velocity jump, respectively, and a 10% density increase at the top of the ULVZ was chosen. Internal velocity gradients (positive and negative) vary. The velocity change across the ULVZ for P wave and S wave velocities are given for the individual traces. (a) Constant ratio of the internal gradients of $\nabla(\delta V_P):\nabla(\delta V_S) = 1:1$. Bottommost gray trace shows ScP precursor double beam. Second lowest trace shows the ULVZ background model without internal ULVZ gradients. (b) Same as Figure 7a but for $\nabla(\delta V_P):\nabla(\delta V_S) = 1:3$.

ULVZ area to the north of the ASAR sampling region. ScP reflection points for the earthquakes that show evidence for multipathing can be found at the southern most edge of the detected ULVZ region. This might indicate that the ULVZ shows a rather sharp boundary around -25.6° latitude. We do not have resolution to the east of the ULVZ region and therefore cannot estimate the exact extension of the ULVZ into that direction. The western boundary of the ULVZ is somewhat clearer defined by two clear nonprecursor detections from R05, indicating a termination of the ULVZ around 166.5° longitude. However, we note that R05 uses a different source-receiver combination, which might influence the detection of the boundary. We estimate that the ULVZ is likely slightly larger than found by R05 with dimensions of about 100 by 100 km.

[25] The ASAR data supports the earlier findings of R05. The reduction of P and S wave velocities and their ratio can be well explained by the existence of 5–30% volume fraction of melt [Williams and Garnero, 1996; Berryman, 2000]. This volume of melt is close to the percolation threshold, but apparently the melt has not separated from the solids present in the ULVZ. A pure molten layer at the CMB is not compatible with the data. Tomographic images for P waves and S waves of this region indicate slower than average seismic velocities in this region [Masters et al., 1996; Grand et al., 1997; Karason and van der Hilst, 2001; Ritsema and van Heijst, 2000], but tomography is not able to resolve structure at the lateral and vertical dimensions targeted in this study. Comparing the location of the detected ULVZ with results from geodynamical modeling [McNamara and Zhong, 2004, 2005], we find that the ULVZ is located just within the edge of a hypothesized large, dense thermochemical pile in the Pacific. These areas

likely contain the highest temperatures in the lowermost mantle, and thus melt might be readily generated in these regions.

[26] The specific elastic parameters, and their possible variation with depth, may be assessed from the velocity and density contrasts derived from our waveform modeling (Figures 9a and 9b). The increase in Poisson's ratio that occurs at the upper boundary of the ULVZ is a natural

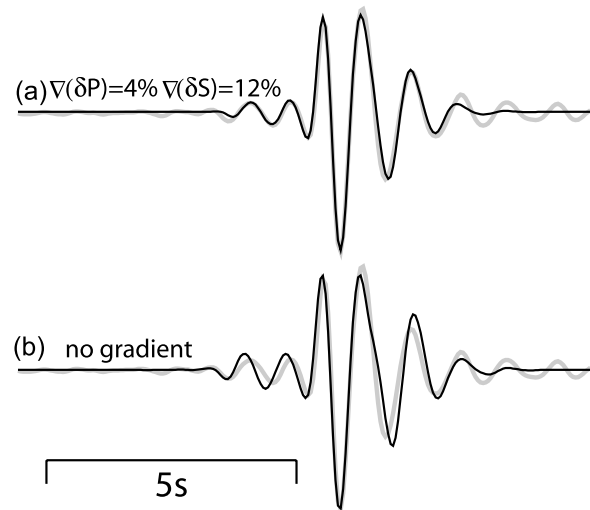


Figure 8. Comparison of waveform fit for models with (a) constant velocity ULVZ and (b) best fitting positive velocity gradient ULVZ model. The best fitting gradient shows a 4% P wave velocity and 12% S wave velocity increase within the ULVZ. For comparison the underlying grey trace shows the double-beam ScP waveform.

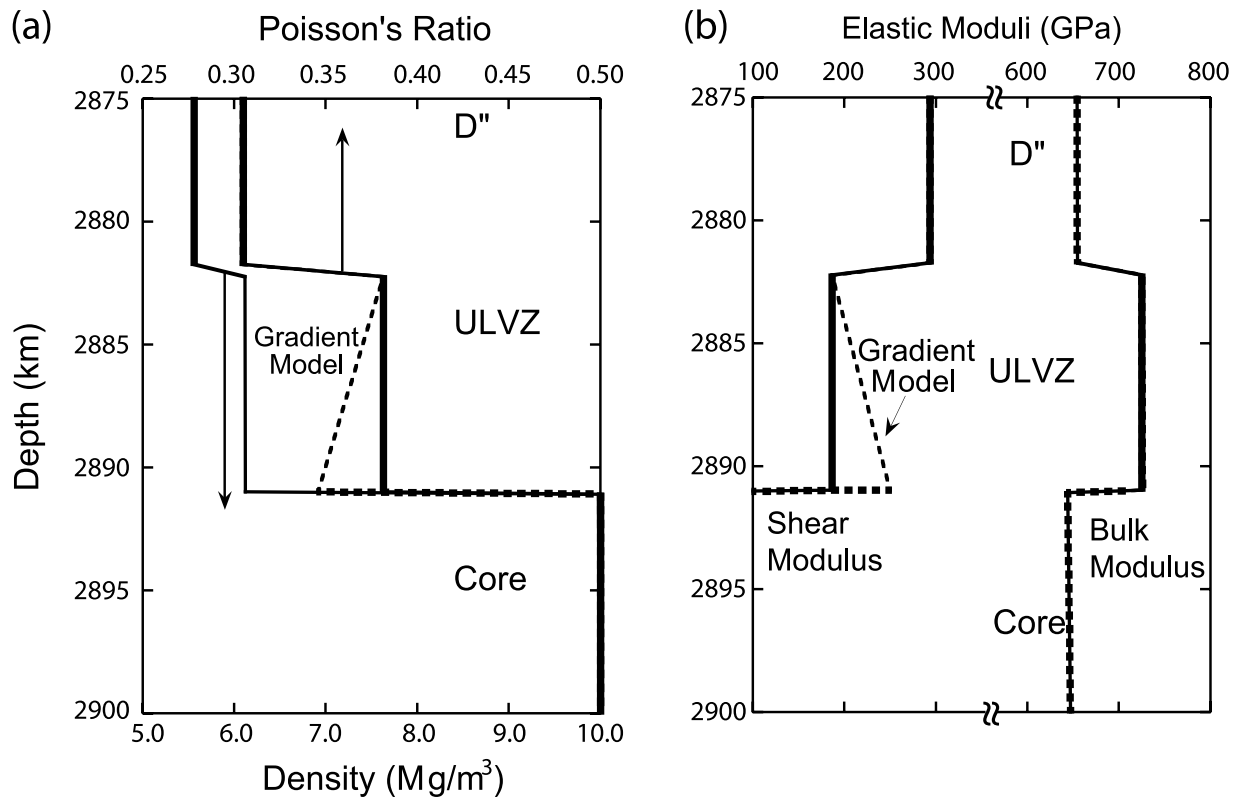


Figure 9. (a) Dependence of density and Poisson's ratio on depth within the ULVZ, as derived from our best fit modeling. Poisson's ratio scale is on the top axis, while the density scale is on the bottom axis. Dotted line shows the model incorporating a velocity gradient within the ULVZ. Arrows point toward the axes relevant to each curve. (b) Dependence of bulk and shear moduli on depth within the ULVZ. The model incorporating a gradient is shown for both bulk and shear modulus (dashed line), but the effect of the velocity gradient on the bulk modulus is essentially negligible relative to the model with a constant velocity within the ULVZ.

consequence of the dramatic decrease in shear velocity associated with this layer (Figure 9a), and is indicative of the likely presence of partial melt within this layer [e.g., Williams and Garnero, 1996; Berryman, 2000]. The variations in the elastic moduli are readily calculable from the tandem modeling of both the density and the compressional and shear velocities for the best fitting model, as shown in Figure 8. The most distinctive aspect of these results is the increase in bulk modulus that occurs within the layer (Figure 9b); this increase is primarily sensitive to the density change associated with the layer, and is almost completely independent of whether or not the ULVZ velocity models contain an internal velocity gradient.

[27] Thus three distinct, but highly interrelated questions emerge concerning the chemistry and phases present within the ULVZ. First, what produces the increased density of this layer? Second, what produces the bulk modulus within this layer that is elevated by $\sim 10\%$ above that of the overlying mantle? Third, what are the likely causes of the possible steep positive velocity gradient within the ULVZ?

[28] The answer to the first question is probably straightforward: the high density of the ULVZ material is most easily generated by iron enrichment in this zone. This does not preclude this zone from being enriched in a range of incompatible elements; rather, iron's abundance and density render it the controlling influence on density. Relative to the

size of the ULVZ density jump, other major mantle constituents, such as calcium and aluminum, have minor effects on density [e.g., Jackson, 1998; Deschamps and Trampert, 2004; Mattern et al., 2005]. Iron might be supplied from the core by material transport through the CMB. Because of the large density difference of the iron, transport from the core into the lowermost mantle is not trivial [Braginsky, 1999], but some mechanisms that might produce some material exchange have been proposed [Jeanloz and Williams, 1998; Petford et al., 2005]. Iron concentration within this zone may have occurred through downward extraction of iron-enriched melts through partial melting processes [Knittle, 1998], possibly coupled with entrainment of core-mantle reaction products into the lowermost mantle [Knittle and Jeanloz, 1991]. Finally, the possibility exists that iron-bearing phases in the deep mantle might unmix at high pressures and temperatures to iron-rich and iron-poor phases, with the former being gravitationally extracted to deep mantle depths [Badro et al., 2003]. This idea has been proposed based on electronic arguments and experimental phase equilibria results [Badro et al., 2003; Dubrovinsky et al., 2000]. However, the experimental results have not been reproduced, and the idea that such unmixing may occur remains highly speculative [Lin et al., 2003].

[29] Both the size of the density increase of the ULVZ relative to that associated to the core and the elevation in

bulk modulus, which is not in accord with simple mixing with core material (Figure 9b), lead us to conclude that the added iron is most likely present as oxidized iron, and predominantly as a FeO component. The magnitude of iron enrichment required to produce a density change of 10% can be assessed from the dependence of density and elasticity on iron content in perovskite and magnesiowustite [e.g., *Mattern et al.*, 2005]: The effects of the postperovskite phase [*Murakami et al.*, 2004] on this exercise are ill constrained but unlikely to be large. For a magnesium perovskite-only ULVZ, a shift in the Fe number ($\text{Fe}/(\text{Fe} + \text{Mg})$ on a molar basis) of near 0.38 would be required. In other words, if a composition near $(\text{Mg}_{0.88}\text{Fe}_{0.12})\text{SiO}_3$ dominated above the ULVZ, then a composition close to $(\text{Mg}_{0.50}\text{Fe}_{0.50})\text{SiO}_3$ would be required to generate a 10% density change. For a ULVZ dominated by magnesiowustite, the corresponding density change would involve a change in Fe number of ~ 0.16 . Compositions with an $(\text{Mg} + \text{Fe})/\text{Si}$ ratio that closely simulates that of pyrolite would clearly have shifts in Fe number between these two extremes.

[30] The question then arises of why (or whether) such a FeO-enriched composition would be anticipated to have an elevated bulk modulus, as shown in Figure 9b. This issue can be examined from the perspective of both the elasticity of iron-enriched melts at high pressures and that of iron-enriched solid phases. If melt is present at the $\sim 20\%$ level within the ULVZ (consistent with our velocity decrements and melt being in noninterconnected inclusions [*Williams and Garnero*, 1996; *Rost et al.*, 2005]), then the elasticity of the melt itself will play a role in modulating the bulk modulus of this layer. The key aspect of the bulk modulus at CMB conditions is its enormously strong dependence on the pressure derivative of the material's bulk modulus (dK/dP or K'): this effect has long been appreciated [*Bullen*, 1949]. There are tantalizing hints that iron-rich and silica-poor melts may have large K' values at modest pressures. *Rigden et al.* [1989] used a phenomenological model to derive a K' of 11.2 for fayalite (Fe_2SiO_4) liquid, and *Agee's* [1992] high-pressure sink float measurements on fayalite liquid yielded a K' of 10.1. However, shock results on fayalite liquid by *Chen et al.* [2002] produced a normal K' value of 5.4 for this material. Simple extrapolation of these elastic results using a third-order Birch-Murnaghan equation of state shows that values of the bulk modulus of an iron-enriched liquid of greater than 700 GPa can be achieved at CMB pressures for zero pressure K' values that are greater than ~ 9.5 . Admittedly, this is a highly uncertain extrapolation. However, this result does imply that an elevated bulk modulus could be partially generated by the presence of silicate melt in the ULVZ.

[31] The bulk moduli of solid, iron-enriched phases at CMB conditions are also uncertain. In this context, the observation of a high spin–low spin transition in $(\text{Mg}_{0.83}\text{Fe}_{0.17})\text{O}$ at 60–70 GPa is likely important [*Badro et al.*, 2003], particularly as such high spin–low spin transitions have been associated with increases in bulk moduli [*Lin et al.*, 2005]. The volume changes associated with these transitions are ill constrained but (depending on iron content) could be between 0 and 2% percent [*Jacobsen et al.*, 2004; *Lin et al.*, 2005]. Moreover, the pressure of the high spin–low spin transition is elevated for more iron-rich

compositions, with the transition in pure FeO not being observed up to CMB pressures [*Badro et al.*, 1999, 2003]. In contrast to the small density changes associated with these transitions, the bulk modulus appears to change quite dramatically. Indeed, the bulk modulus of $(\text{Mg}_{0.83}\text{Fe}_{0.17})\text{O}$ is elevated by $\sim 35\%$ within, due to the high spin–low spin transition [*Lin et al.*, 2005]. Such behavior is in complete accord with the long-recognized gross correlation between decreased ionic volumes and increased bulk moduli [e.g., *Anderson and Nafe*, 1965]. Accordingly, while the bulk modulus of perovskite and magnesiowustite change little as a function of high-spin iron substituting for magnesium [e.g., *Mattern et al.*, 2005], low-spin iron is probably associated with a markedly increased bulk modulus, and the elevated bulk modulus within the ULVZ could be a natural consequence of the elevated iron content in this layer. Thus the presence of iron-enriched material containing low spin iron within the solid matrix of the ULVZ provides a natural and self-consistent explanation for both the increased bulk modulus and density that we observe within this layer.

[32] While both the elevated bulk modulus and density of the ULVZ may be attributed to moderate iron enrichment, it is the velocity decrements themselves that require the presence of partial melt. A decrease in compressional wave velocity of 8% would require a notably larger iron content than is dictated by our $\sim 10\%$ density change [*Mao et al.*, 2005; *Stackhouse et al.*, 2006]. Indeed, current estimates of the effect of iron on the shear velocity of the postperovskite phase show that a 24% decrease in shear velocity is impossible to approach with iron contents compatible with our constraints on the density of this zone [*Mao et al.*, 2005; *Stackhouse et al.*, 2006]. Indeed, the magnitude of velocity changes produced by an iron content sufficient to generate a 10% density contrast for solid postperovskite are near -6% in compressional wave velocity and -10% in shear velocity [*Stackhouse et al.*, 2006]. While determining the tandem effects of moderate iron enrichment and different amounts and textures of partial melt on velocity decrements at CMB conditions is subject to a broad range of uncertainties, there are robust observations that can be made. First, a 3 to 1 ratio of $d\ln V_s$ to $d\ln V_p$ remains strongly indicative of the presence of partial melt [*Williams and Garnero*, 1996; *Berryman*, 2000]. Second, the presence of elevated iron content reduces the amount of partial melt inferred to be present within the ULVZ based on the observed velocity decrements. For example, for spherical melt inclusions, the inferred amount of partial melt required to generate the observed decrements of velocity is decreased from in excess of 20% to $\sim 14\%$ by the presence of sufficient iron to generate a 10% density increase. The key point here is simply that the velocity decrements (and particularly those involving shear velocity) of the ULVZ may be generated straightforwardly by partial melting at depth. Moderately elevated iron contents can enhance these decrements. However, the proposition that added iron alone can generate ULVZ's [*Mao et al.*, 2005; *Stackhouse et al.*, 2006] requires analysis in terms of not only accurately determined compressional and shear wave velocities within these zones, but also constraints on their density as well: in short, information of the type that this study provides.

[33] The possibility that a strong positive velocity gradient exists within the ULVZ is most easily explained in terms of shifts in either the amount or distribution of melt as a function of depth. Figure 10 shows two examples of possible melt contents for both a constant velocity model for the ULVZ, and three melt distributions that could give rise to a positive gradient. As discussed by R05, the maintenance of partial melt within the ULVZ is most easily explained by a zone containing nonconnecting melts near the CMB. Unless the density contrast between melt and coexisting solid is negligible, melt segregation (likely downward) would be anticipated if the melts were interconnected. Yet, if melt is derived from the mantle above and descends via negative buoyancy into the ULVZ, as proposed by R05, then a shift in melt texture is anticipated in the lowermost reaches of the mantle from connected (or wetting) melt to isolated pockets near the CMB.

[34] A positive velocity gradient could be simply associated with a change in melt fraction, as in the right dashed line in Figure 10, in which the melt content in spherical pockets is higher near the top of the ULVZ and decreases through its depth. Such a scenario would imply that melt content does not simply increase with temperature, as the base of the ULVZ is almost certainly hotter than the top. Moreover, if melts are negatively buoyant, the rationale for having a decrease in melt content as a function of depth is unclear.

[35] The thermal constraint on having more melt at deeper, presumably higher temperature regions in the ULVZ is compatible with a positive velocity gradient if a change in melt texture occurs; the single positively sloped dotted line in Figure 10 shows such a gradient for a progressive transition from all the melt at the top of the ULVZ being present as interconnected sheets with an aspect ratio of 0.01, to all the melt being present in spherical inclusions at its base. Clearly, the genesis of any positive gradient within the ULVZ hinges critically on the precise texture of the melt; moreover, positive gradients absolutely do not need to be associated with a decrease in melt content as a function of depth. From a dynamic perspective, a picture of downward percolative flow dominating at shallower levels deep within D'' and recharging (or indeed, simply transporting) melt into the ULVZ, and the melt progressively reacting with the surrounding solids to generate a low-permeability framework that can maintain partial melt within the ULVZ has considerable correlation with magmatic processes near the surface. In effect, this picture bears considerable resemblance to an upside-down near-surface magma chamber.

6. Conclusions

[36] Using high-frequency ScP array recordings data allows a improved resolution of ULVZ location and structure. The studied patch shows a very good coverage with ScP reflection points due to the deep seismic activity along the Tonga-Fiji and Vanuatu subduction zones. The larger vertical resolution of the high-frequency data, due to shorter wavelengths, also allows some insight into the chemistry of the ULVZ, and the dynamics of its development. We find that the most parsimonious explanation for the elevated density and bulk modulus of the ULVZ likely involves enrichment in low-spin iron oxide; a Fe/Mg ratio of between

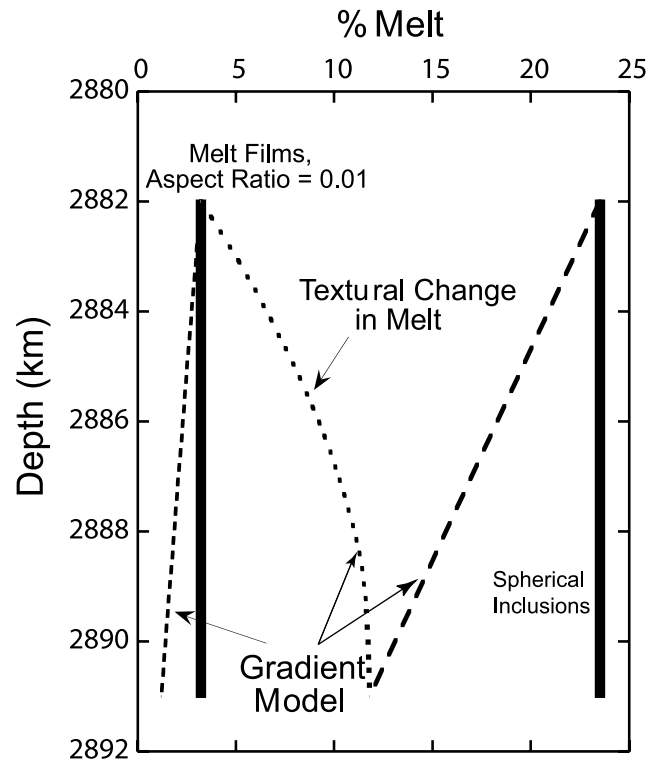


Figure 10. A range of possible melt distributions within the ULVZ, calculated using the methods outlined by *Williams and Garnero* [1996]. Bold vertical lines represent constant melt distributions that could generate the velocity depressions associated with the ULVZ for the case of spherical melt inclusions (right vertical line) and melt films with aspect ratios of 0.01 (left vertical line). The straight dashed lines represent melt distributions that can generate a positive velocity gradient of +4% in compressional wave velocity and +12% in shear wave velocity within the ULVZ itself, with the left dashed line being associated with melt films, and the right straight dotted line being for spherical inclusions. The curved dotted line denotes the variation in melt fraction that could explain a positive velocity gradient within the ULVZ if the melt undergoes a textural change from being present within films at the top of the ULVZ to being present in spherical pockets at the core-mantle boundary.

1 and 0.35 (depending on silica content) can produce the best fit density of this region. Similarly, if low-spin iron is associated with large incompressibilities, as is indicated by both, simple systematics and recent measurements, then the increased bulk modulus of this region may be a secondary consequence of its iron enrichment. The velocity gradient within the ULVZ is likely positive, and could be fairly large. Such a gradient could be generated by an increased amount of melt as a function of depth within the ULVZ, but with a transition in its textural characteristics: from a wetting melt near the top of the ULVZ, as melt descends (and perhaps ponds) at the top of the ULVZ from the overlying mantle, to a zone with isolated inclusions of melt juxtaposed with the core itself.

[37] To better understand the dynamics and evolution of ULVZ and their role in mantle dynamics a more global characterization of ULVZ distribution and structure is necessary. Data from small-aperture arrays a well suited for this task and will be used in a future study to sample larger areas of the Earth's CMB.

[38] **Acknowledgments.** Data were processed with SeismicHandler [Stammler, 1993]. Figures were produced using GMT [Wessel and Smith, 1998]. Comments by Y. Fei and two anonymous reviewers helped greatly to improve the manuscript. We thank the Center for Monitoring Research for the Alice Springs data. This work is supported by NSF grants EAR-0135119 (E.G.), EAR-0310342 (Q.W.), and NSF CSEDI grant EAR-0456356 (S.R.).

References

- Agee, C. B. (1992), Isothermal compression of molten Fe_2SiO_4 , *Geophys. Res. Lett.*, **19**, 1169–1172.
- Anderson, O. L., and J. E. Nafe (1965), The bulk modulus-volume relationship for oxide compounds and related geophysical problems, *J. Geophys. Res.*, **70**, 3951–3962.
- Badro, J., V. V. Struzhkin, J. Shu, R. J. Hemley, H. K. Mao, C. C. Kao, J. P. Rueff, and G. Shen (1999), Magnetism in FeO at megabar pressures from X-ray emission spectroscopy, *Phys. Rev. Lett.*, **83**, 4101–4104.
- Badro, J., G. Fiquet, F. Guyot, J. P. Rueff, V. V. Struzhkin, G. Vanko, and G. Monaco (2003), Iron partitioning in Earth's mantle: Toward a deep lower mantle discontinuity, *Science*, **300**, 789–791.
- Bataille, K., and F. Lund (1996), Strong scattering of short-period seismic waves by the core-mantle boundary and the P-diffracted wave, *Geophys. Res. Lett.*, **23**, 2413–2416.
- Berryman, J. G. (2000), Seismic velocity decrement ratios for regions of partial melt in the lower mantle, *Geophys. Res. Lett.*, **27**, 421–424.
- Braginsky, S. I. (1999), Dynamics of the stably stratified ocean at the top of the core, *Phys. Earth Planet. Inter.*, **111**, 21–34.
- Buffett, B. A., E. J. Garnero, and R. Jeanloz (2000), Sediments at the top of Earth's core, *Science*, **290**, 1338–1342.
- Bullen, K. E. (1949), Compressibility-pressure hypothesis and the Earth's interior, *Mon. Not. R. Astron. Soc., Geophys. Suppl.*, **5**, 355–368.
- Castle, J. C., and R. D. van der Hilst (2000), The core-mantle boundary under the Gulf of Alaska: No ULVZ for shear waves, *Earth Planet. Sci. Lett.*, **176**, 311–321.
- Cerveny, V., M. M. Popov, and I. Psencik (1982), Computation of wave fields in inhomogeneous-media Gaussian-beam approach, *Geophys. J. R. Astron. Soc.*, **70**, 109–128.
- Chen, G. Q., T. J. Ahrens, and E. M. Stolper (2002), Shock-wave equation of state of molten and solid fayalite, *Phys. Earth Planet. Inter.*, **134**, 25–32.
- Deschamps, F., and J. Trampert (2004), Towards a lower mantle reference temperature and composition, *Earth Planet. Sci. Lett.*, **222**, 161–175.
- Dubrovinsky, L. S., N. A. Dubrovinskaia, S. K. Saxena, H. Annersten, E. Halenius, H. Harryson, F. Tutti, S. Rekhii, and T. Le Bihan (2000), Stability of ferropericline in the lower mantle, *Science*, **289**, 430–432.
- Dziewonski, A. M., and D. L. Anderson (1981), Preliminary Reference Earth Model, *Phys. Earth Planet. Inter.*, **25**, 297–356.
- Garnero, E. J. (2000), Heterogeneity of the lowermost mantle, *Annu. Rev. Earth Planet. Sci.*, **28**, 509–537.
- Garnero, E. J., and D. V. Helmberger (1998), Further structural constraints and uncertainties of a thin laterally varying ultralow-velocity layer at the base of the mantle, *J. Geophys. Res.*, **103**, 12,495–12,509.
- Garnero, E. J., and J. E. Vidale (1999), *ScP*: A probe of ultralow velocity zones at the base of the mantle, *Geophys. Res. Lett.*, **26**, 377–380.
- Garnero, E., J. Revenaugh, Q. Williams, T. Lay, and L. H. Kellogg (1998), Ultralow velocity zone at the core-mantle boundary, in *The Core-Mantle Boundary Region, Geodyn. Ser.*, vol. 28, edited by M. Gurnis et al., pp. 319–334, AGU, Washington, D. C.
- Given, H., et al. (2000), The primary seismic network, international monitoring system, paper presented at 22nd Annual DoD/DOE Seismic Research Symposium, New Orleans, La.
- Grand, S. P., R. D. van der Hilst, and S. Widiyantoro (1997), Global seismic tomography: a snapshot of convection in the Earth, *GSA Today*, **7**, 1–7.
- Hernlund, J. W., C. Thomas, and P. J. Tackley (2005), A doubling of the post-perovskite phase boundary and structure of the Earth's lowermost mantle, *Nature*, **434**, 882–886.
- Jackson, I. (1998), Elasticity, composition and temperature of the Earth's lower mantle: A reappraisal, *Geophys. J. Int.*, **134**, 291–311.
- Jacobsen, S. D., H. Spetzler, H. J. Reichmann, and J. R. Smyth (2004), Shear waves in the diamond-anvil cell reveal pressure-induced instability in (Mg, Fe)O, *Proc. Natl. Acad. Sci. U.S.A.*, **101**, 5867–5871.
- Jeanloz, R., and Q. Williams (1998), The core-mantle boundary region, *Rev. Mineral.*, **37**, 241–259.
- Karason, H., and R. D. van der Hilst (2001), Tomographic imaging of the lowermost mantle with differential times of refracted and diffracted core phases (PKP, Pdiff), *J. Geophys. Res.*, **106**, 6569–6587.
- Kendall, J.-M. (2000), Seismic anisotropy in the boundary layers of the mantle, in *Earth's Deep Interior: Mineral Physics and Tomography From the Atomic to the Global Scale, Geophys. Monogr. Ser.*, vol. 117, edited by S. Karato et al., pp. 149–175, AGU, Washington, D. C.
- Kendall, J.-M., and P. Silver (1998), Investigating Causes of D'' Anisotropy, in *The Core-Mantle Boundary Region, Geodyn. Ser.*, vol. 28, edited by M. Gurnis et al., pp. 97–118, AGU, Washington, D. C.
- Knittle, E. (1998), The solid/liquid partitioning of major and radiogenic elements at lower mantle pressures: Implications for the core-mantle boundary region, in *The Core-Mantle Boundary Region, Geodyn. Ser.*, vol. 28, edited by M. Gurnis et al., pp. 119–130, AGU, Washington, D. C.
- Knittle, E., and R. Jeanloz (1991), The Earth's core-mantle boundary: Results of experiments at high pressures and temperatures, *Science*, **251**, 1438–1443.
- Koper, K. D., and M. L. Pyle (2004), Observations of PKiKP/PcP amplitude ratios and implications for Earth structure at the boundaries of the liquid core, *J. Geophys. Res.*, **109**, B03301, doi:10.1029/2003JB002750.
- Kradolfer, U. (1993), Automating the exchange of earthquake information, *Eos Trans. AGU*, **74**, 442, 444–445.
- Lay, T., and E. J. Garnero (2004), Core-mantle boundary structures and processes, in *The State of the Planet: Frontiers and Challenges in Geophysics, Geophys. Monogr. Ser.*, vol. 150, edited by R. S. J. Sparks, and C. J. Hawkesworth, pp. 25–41, AGU, Washington, D. C.
- Lay, T., and D. V. Helmberger (1983), A lower mantle S-wave triplication and the shear velocity structure of D'' , *Geophys. J. R. Astron. Soc.*, **75**, 799–837.
- Lay, T., Q. Williams, E. Garnero, L. H. Kellogg, and M. E. Wyssession (1998), Seismic wave anisotropy in the D'' region and its implications, in *The Core-Mantle Boundary Region, Geodyn. Ser.*, vol. 28, edited by M. Gurnis et al., pp. 299–318, AGU, Washington, D. C.
- Lay, T., E. J. Garnero, and S. A. Russell (2004), Lateral variation of the D'' discontinuity beneath the Cocos Plate, *Geophys. Res. Lett.*, **31**, L15612, doi:10.1029/2004GL020300.
- Lay, T., D. Heinz, M. Ishii, S.-H. Shim, J. Tsuchiya, T. Tsuchiya, R. Wentzcovitch, and D. Yuen (2005), Multidisciplinary impact of the deep mantle phase transitions in perovskite structure, *Eos Trans. AGU*, **86**, 1, 5.
- Lin, J. F., D. L. Heinz, H. K. Mao, R. J. Hemley, J. M. Devine, J. Li, and G. Shen (2003), Stability of magnesiowustite in Earth's lower mantle, *Proc. Natl. Acad. Sci. U.S.A.*, **100**, 4405–4408.
- Lin, J. F., V. V. Struzhkin, S. D. Jacobsen, M. Y. Hu, P. Chow, J. Kung, H. Liu, H. K. Mao, and R. J. Hemley (2005), Spin transition of iron in magnesiowustite in the Earth's lower mantle, *Nature*, **436**, 377–380.
- Mao, W. L., et al. (2005), Iron-rich silicates in the Earth's D'' layer, *Proc. Natl. Acad. Sci. U.S.A.*, **102**, 9751–9753.
- Masters, G., S. Johnson, G. Laske, and H. Bolton (1996), A shear-velocity model of the mantle, *Philos. Trans. R. Soc. London, Ser. A*, **354**, 1385–1410.
- Masters, G., G. Laske, H. Bolton, and A. M. Dziewonski (2000), The relative behavior of shear velocity, bulk sound speed, and compressional velocity in the mantle: Implications for chemical and thermal structure, in *Earth's Deep Interior: Mineral Physics and Tomography From the Atomic to the Global Scale, Geophys. Monogr. Ser.*, vol. 117, edited by S. Karato et al., pp. 63–87, AGU, Washington, D. C.
- Mattern, E., J. Matas, Y. Ricard, and J. Bass (2005), Lower mantle composition and temperature from mineral physics and thermodynamic modeling, *Geophys. J. Int.*, **160**, 973–990.
- McNamara, A. K., and S. Zhong (2004), Thermochemical structures within a spherical mantle: Superplumes or piles?, *J. Geophys. Res.*, **109**, B07402, doi:10.1029/2003JB002847.
- McNamara, A. K., and S. J. Zhong (2005), Thermochemical structures beneath Africa and the Pacific Ocean, *Nature*, **437**, 1136–1139.
- Müller, G. (1985), The reflectivity method: A tutorial, *Z. Geophys.*, **58**, 153–174.
- Murakami, M., K. Hirose, K. Kawamura, N. Sata, and Y. Ohishi (2004), Post-perovskite phase transition in MgSiO_3 , *Science*, **304**, 855–858.
- Ni, S. D., E. Tan, M. Gurnis, and D. Helmberger (2002), Sharp sides to the African superplume, *Science*, **296**, 1850–1852.
- Ni, S. D., D. V. Helmberger, and J. Tromp (2005), Three-dimensional structure of the African superplume from waveform modelling, *Geophys. J. Int.*, **161**, 283–294.
- Oganov, A. R., and S. Ono (2004), Theoretical and experimental evidence for a post-perovskite phase of MgSiO_3 in Earth's D'' layer, *Nature*, **430**, 445–448.

- Persh, S. E., J. E. Vidale, and P. S. Earle (2001), Absence of short-period ULVZ precursors to *PcP* and *ScP* from two regions of the CMB, *Geophys. Res. Lett.*, *28*, 387–390.
- Petford, N., D. Yuen, T. Rushmer, J. Brodholt, and S. Stackhouse (2005), Shear-induced material transfer across the core-mantle boundary aided by the post-perovskite phase transition, *Earth Planets Space*, *57*, 459–464.
- Reasoner, C., and J. Revenaugh (2000), *ScP* constraints on ultralow-velocity zone density and gradient thickness beneath the Pacific, *J. Geophys. Res.*, *105*, 28,173–28,182.
- Revenaugh, J., and R. Meyer (1997), Seismic evidence of partial melt within a possibly ubiquitous low-velocity layer at the base of the mantle, *Science*, *277*, 670–673.
- Rigden, S. M., T. J. Ahrens, and E. M. Stolper (1989), High-pressure equation of state of molten anorthite and diopside, *J. Geophys. Res.*, *94*, 9508–9522.
- Ritsema, J., and H.-J. van Heijst (2000), Seismic imaging of structural heterogeneity in earth's mantle: Evidence for large-scale mantle flow, *Sci. Progr.*, *83*, 243–259.
- Rondenay, S., and K. M. Fischer (2003), Constraints on localized core-mantle boundary structure from multichannel, broadband *SKS* coda analysis, *J. Geophys. Res.*, *108*(B11), 2537, doi:10.1029/2003JB002518.
- Rost, S., and E. J. Garnero (2005), Array seismology advances research into Earth's interior, *Eos Trans. AGU*, *85*, 301, 305–306.
- Rost, S., and J. Revenaugh (2001), Seismic detection of rigid zones at the top of the core, *Science*, *294*, 1911–1914.
- Rost, S., and J. Revenaugh (2003), Small-scale ultralow-velocity zone structure imaged by *ScP*, *J. Geophys. Res.*, *108*(B1), 2056, doi:10.1029/2001JB001627.
- Rost, S., and C. Thomas (2002), Array seismology: Methods and applications, *Rev. Geophys.*, *40*(3), 1008, doi:10.1029/2000RG000100.
- Rost, S., E. J. Garnero, Q. Williams, and M. Manga (2005), Seismological constraints on a possible plume root at the core-mantle boundary, *Nature*, *435*, 666–669.
- Stackhouse, S., J. P. Brodholt, and G. D. Price (2006), Elastic anisotropy of FeSiO₃ end-members of the perovskite and post-perovskite phases, *Geophys. Res. Lett.*, *33*, L01304, doi:10.1029/2005GL023887.
- Stammler, K. (1993), SeismicHandler: Programmable multichannel data handler for interactive and automatic processing of seismological analyses, *Comput. Geosci.*, *19*, 135–140.
- Thomas, C., M. Weber, A. Agnon, and A. Hofstetter (1998), A low-velocity lamella in D'', *Geophys. Res. Lett.*, *25*, 2885–2888.
- Thorne, M. S., and E. J. Garnero (2004), Inferences on ultralow-velocity zone structure from a global analysis of *SPdKS* waves, *J. Geophys. Res.*, *109*, B08301, doi:10.1029/2004JB003010.
- Vidale, J. E., and H. Benz (1992), A sharp and flat section of the core-mantle boundary, *Nature*, *359*, 627–629.
- Vidale, J. E., and M. A. H. Hedlin (1998), Evidence for partial melt at the core-mantle boundary north of Tonga from the strong scattering of seismic waves, *Nature*, *391*, 682–685.
- Weber, M. (1988), Computation of body-wave seismograms in absorbing 2-D media using the Gaussian-beam method: Comparison with exact methods, *Geophys. J.*, *92*, 9–24.
- Wessel, P., and W. H. F. Smith (1998), New, improved version of the Generic Mapping Tools released, *Eos Trans. AGU*, *79*, 579.
- Williams, Q., and E. J. Garnero (1996), Seismic evidence for partial melt at the base of Earth's mantle, *Science*, *273*, 1528–1530.
- Wysession, M. E. (1996), Imaging cold rock at the base of the mantle: The sometimes fate of slabs?, in *Subduction: Top to Bottom*, *Geophys. Monogr. Ser.*, vol. 96, edited by G. E. Bebout et al., pp. 369–384, AGU, Washington, D. C.
- Wysession, M. E., T. Lay, J. Revenaugh, Q. Williams, E. J. Garnero, R. Jeanloz, and L. H. Kellogg (1998), The D'' discontinuity and its implications, in *The Core-Mantle Boundary Region*, *Geodyn. Ser.*, vol. 28, edited by M. Gurnis et al., pp. 273–298, AGU, Washington, D. C.
- Zhao, D. (2001), Seismic structure and origin of hotspots and mantle plumes, *Earth Planet. Sci. Lett.*, *192*, 251–265.

E. J. Garnero, Department of Geological Sciences, Arizona State University, Box 871404, Tempe, AZ 85287-1404, USA.

S. Rost, School of Earth and Environment, University of Leeds, Leeds LS 29JT, UK. (earsro@earth.leeds.ac.uk)

Q. Williams, Department of Earth Sciences, University of California, 1156 High St., Santa Cruz, CA 95064, USA.